OPEN ACCESS



Anisotropy of Density Fluctuations in the Solar Wind at 1 au

Abstract

A well-known property of solar wind plasma turbulence is the observed anisotropy of the autocorrelations, or equivalently the spectra, of velocity and magnetic field fluctuations. Here we explore the related but apparently not well-studied issue of the anisotropy of plasma density fluctuations in the energy-containing and inertial ranges of solar wind turbulence. Using 10 yr (1998–2008) of in situ data from the Advanced Composition Explorer mission, we find that for all but the fastest wind category, the density correlation scale is slightly larger in directions quasiparallel to the large-scale mean magnetic field as compared to quasi-perpendicular directions. The correlation scale in fast wind is consistent with isotropic. The anisotropy as a function of the level of correlation is also explored. We find at small correlation levels, i.e., at energy-containing scales and larger, the density fluctuations are close to isotropy for fast wind, and slightly favor more rapid decorrelation in perpendicular directions for slow and medium winds. At relatively smaller (inertial range) scales where the correlation values are larger, the sense of anisotropy is reversed in all speed ranges, implying a more "slablike" structure, especially prominent in the fast wind samples. We contrast this finding with published results on velocity and magnetic field correlations.

Unified Astronomy Thesaurus concepts: Interplanetary turbulence (830); Space plasmas (1544); Plasma physics (2089); Solar wind (1534); Magnetohydrodynamics (1964)

1. Introduction

There are two well-known reasons for turbulent fluctuations in the solar wind to exhibit departures from statistical isotropy (Batchelor 1970; Oughton et al. 2015). The first is solar wind expansion, which in the simplest terms imposes the radial coordinate as a preferred direction. This is expected to influence mainly those structures larger than the turbulence correlation scales. For smaller-scale structures, including the inertial and kinetic ranges, the second influence—that of the local large-scale magnetic field—is expected to exert a dominant influence. Indeed, it is well established that in the inertial range of magnetohydrodynamic (MHD) turbulence, the correlation functions (or equivalently, the spectra) of magnetic field and velocity fluctuations exhibit anisotropy relative to the magnetic field direction (Matthaeus et al. 1990, 1996; Shaikh & Zank 2010; Chen et al. 2012; Oughton et al. 2015). The symmetries that may be associated with this anisotropy may be referred to as rotational symmetries, such as axisymmetric "slab" or "2D" geometries (Bieber et al. 1996). The analogous issue of anisotropy of density fluctuations has received some attention, reviewed below, in the theoretical and numerical simulation literature (Matthaeus et al. 1996; Chandran & Backer 2002; Cho & Lazarian 2002; Zank et al. 2012) as well as in remote sensing observations (Coles & Harmon 1989). However, to our knowledge, the issue of correlation or spectral anisotropy of the density fluctuation field in the energycontaining and inertial ranges of turbulence has not been fully

Original content from this work may be used under the terms of the Creative Commons Attribution 4.0 licence. Any further distribution of this work must maintain attribution to the author(s) and the title of the work, journal citation and DOI.

examined in solar wind in situ observations. Here we take a step in that direction by examining density correlation statistics, their variation relative to the mean magnetic field and their variation with scale. (Mean values and other statistics are computed over samples of at least a correlation scale, in accord with classical ergodic theory; see e.g., Panchev 1971.) As in the usual picture of turbulence, scales can be categorized as the energy-containing, inertial, and dissipation regimes. Here, we focus on the former two, which are roughly separated by the correlation scale (Frisch 1995). Our study emphasizes observations near 1 au, where long-term data sets provide the possibility of high statistical weight analyses.

Coronal and solar wind density fluctuations can be studied based on remote sensing techniques, such as analysis of scintillation of signals from distant radio sources (Coles & Harmon 1989; Armstrong et al. 1990; Kellogg & Horbury 2005; Kontar et al. 2023). Rotational symmetry is frequently extracted from these measurements. Many of these studies are designed to detect coronal density properties, while a few have been carried out near 1 au. The seminal work of Celnikier et al. (1987) describes the limitations and sensitivities of this class of scintillation studies. A typical conclusion is that structures in the coronal density fluctuation field are preferentially elongated in the direction of the inferred mean magnetic field. This implies that density gradients are stronger in directions perpendicular to the magnetic field. This sense of correlation anisotropy is familiar in solar wind measurements of velocity and magnetic field (Matthaeus et al. 1990; Bieber et al. 1996; Hamilton et al. 2008; Narita et al. 2010; Chen et al. 2011; Horbury et al. 2012; Oughton et al. 2015).

Interplanetary density spectra have also been examined based on in situ observations (see, e.g., Bellamy et al. 2005).

But the directional dependence of density fluctuation statistics in the inertial and energy-containing ranges of scales have sometimes been overlooked, even in relatively complete characterizations of turbulence correlations (Borovsky 2012). When density fluctuations have been considered, the emphasis has often been on high-frequency or subion scales (Celnikier et al. 1987; Malaspina et al. 2010; Chen et al. 2013; Kontar et al. 2023) where kinetic plasma properties are probed. However, we are not aware that a comprehensive survey has been carried out to describe the anisotropy of MHD-scale inertial range correlation of the plasma density. This motivates our current focus on the anisotropy of energy-containing range and inertial range density fluctuations near Earth's orbit.

This paper is organized as follows: in Section 2 we discuss the "Maltese cross" representation of correlation anisotropy, which serves as the theoretical basis prompting this research. In Section 3 we describe our data and analysis procedure. Section 4 presents our results on the scale-dependent density correlation anisotropy, and Section 5 discusses the implications of the results.

2. Simplified Representations of Anisotropy

A point of reference that motivates the present study is the "Maltese cross" autocorrelation pattern (Matthaeus et al. 1990) derived from the interplanetary magnetic field at 1 au. The pattern is assumed to be axisymmetric about the mean magnetic field \mathbf{B}_0 and consists of a lobe that admits gradients mainly in the direction parallel to \mathbf{B}_0 and another part that varies mainly in the directions perpendicular to \mathbf{B}_0 . In an idealized sense, the former are known as "slab" fluctuations, and the latter, "2D" fluctuations. This so-called two-component model has become a useful parameterization for anisotropy that incorporates both Alfvén wavelike spectral components and a quasi-2D (Q2D) ingredient that varies, at most, weakly along a mean field (Bieber et al. 1994, 1996). The two-component parameterization allows for arbitrary admixtures of energy in models that vary mainly along or transverse to the mean field, and as such has become a convenient and often-invoked model for use in theoretical work on charged particle scattering (Zank et al. 2004; Shalchi 2009; Shalchi et al. 2010; Zhao et al. 2017, 2018). It is also incorporated with several variations into turbulence transport models that describe turbulence throughout the heliosphere as well as models for solar wind acceleration and evolution in the presence of turbulence (e.g., Adhikari et al. 2017; Usmanov et al. 2018). The anisotropy present in such models exerts a strong influence on the results of such calculations and modeling of turbulence. It is essential to bear in mind that such parameterization of anisotropy are crude representations, and are not intended as dynamical turbulence models. However, they demonstrate the physical significance and impact of correlation or spectral anisotropy.

Another approach to describing spectral anisotropy is based on wave theory, with the premise being that linear MHD wave modes may be separated unambiguously based on their polarization properties (Cho & Lazarian 2002; Cho et al. 2002). (The standard decomposition has been controversial for some time and recently a more complete approximate representation that includes structures as well as waves has been suggested by Zank et al. 2023.) This wave decomposition idea can be directly carried over to turbulence in the weak turbulence regime. In that case, the adopted basis and leading-order dynamical solutions are constructed from the linear

modes themselves (Chandran 2005). In this view, the Alfvén mode is anisotropic, a well-established property in strong MHD turbulence (Shebalin et al. 1983; Oughton et al. 1994). In addition, the Alfvén mode is polarized transverse to the mean magnetic field, a small-amplitude property adopted in critical balance theory by Goldreich & Sridhar (1995; see also Oughton & Matthaeus 2020). The slow mode is assumed to follow a passive dynamics, and to admit an anisotropy similar to the incompressible Alfvén mode. The decomposition into wave modes is completed by extracting fluctuations with the polarization of linear fast modes. These remain isotropic, as the fast mode dispersion does not depend on direction. It is widely regarded that useful results have been attained based on a linear-wave decomposition. However, it should be disparaged as a general representation of MHD turbulence, as it has been shown to be essentially incomplete (Zank et al. 2023); in particular it lacks coherent structures and nonpropagating structures that are nonetheless found to be dynamically important (Gan et al. 2022; Zhao et al. 2023).

The linear-wave theory underlies a popular surrogate for compressional effects, the so-called magnetic compressibility, that has been extensively employed in observational solar wind studies (Chen et al. 2012; Bruno & Carbone 2013). This surrogate assumes that the relative strength of the component of the magnetic variance parallel to the ambient (mean) magnetic field is a measure of compressional dynamical activity. This assumption breaks down for large-amplitude turbulence, wherein parallel fluctuations need not be identified with compressional fast magnetosonic modes. Such fluctuations could have a more general character, such as an indication of spherical polarization of large-amplitude Alfvénic fluctuations (Barnes & Hollweg 1974; Barnes 1981), which are usually not associated with density variations.

In the following, we will not make explicit use of representations based on mode decomposition, but rather will incorporate the underlying ideas into our physical discussion of the anisotropy of solar wind density fluctuations.

3. Data and Analysis Procedure

We acquire 10 yr (from 1998 February to 2008 March) of ion number density data observed by the SWEPAM instrument on the Advanced Composition Explorer (ACE) spacecraft (McComas et al. 1998), along with corresponding solar wind speed measurements from SWEPAM and magnetic field measurements from the magnetic field instrument (MAG; Smith et al. 1998) on ACE. This data set covers most of a solar activity cycle, with maximum sunspot number occurring in 2003 (e.g., Balmaceda et al. 2009). The original data at 64 s resolution is upsampled to a 1 minute cadence and separated into data sets that span 1 day. Overlapping midnight-tomidnight and noon-to-noon intervals are included to increase the total number of data sets and suppress systematic daytimescale periodicities. We remove interplanetary coronal mass ejections (ICMEs) from the data samples, under the assumption that their characteristic average plasma properties relegate them to a distinct class of wind intervals (Klein & Burlaga 1982; Cane & Richardson 2003) that we do not consider here; for this, we consulted an available online table of ICMEs (Richardson & Cane 2024). About 11% of intervals with wind speeds below 400 km s⁻¹ are removed, while approximately 15% are removed for wind speeds surpassing 400 km s⁻¹. The difference may be attributed to the prevalence of ICMEs during

Table 1
ACE 24 hr Data Set Count in Each Wind Speed and Angular Channel

-	\leq 400 km s ⁻¹	400–500 km s ⁻¹	\geqslant 500 km s ⁻¹
0°-40°	62	81	34
40°–45°	96	97	77
45°-50°	206	283	284
50°-55°	341	487	563
55°-60°	449	621	492
60°-65°	373	400	227
65°-90°	392	265	81
Total	1919	2234	1758

Note. The angle θ is defined in Equation (1).

the solar maximum, particularly when fast solar winds are more abundant within the ecliptic plane. In addition, a density interval is discarded if over 70% of the observations are empty. Within the retained intervals, any missing data—necessarily less than 70% of the span of the interval is marked "NAN" to exclude it from our computations. We then compute a linear least-squares fit to each interval, and detrend the interval by subtracting the fit from the data, resulting in zero-mean data samples.

We group the data intervals based on their mean solar wind speed $V_{\rm SW}$ and the angle between their mean magnetic and velocity fields:

$$\theta = \cos^{-1} \left(\frac{\langle \tilde{\mathbf{B}} \rangle \cdot \langle \tilde{\mathbf{V}}_{SW} \rangle}{\langle |\mathbf{B}| \rangle \langle |\mathbf{V}_{SW}| \rangle} \right) \tag{1}$$

where the tilde notation $\tilde{\bf A}$ indicates computing the absolute value of each component of a vector ${\bf A}$, and $\langle \cdots \rangle$ refers to averaging over an individual 24 hr data set. Taking the absolute value effectively avoids the cancellation of θ within a given interval due to magnetic polarity reversals. The θ channels are 0°-40°, 40°-45°, 45°-50°, 50°-55°, 55°-60°, 60°-65°, and 65°-90°, and the $V_{\rm SW}$ channels are 0-400, 400-500, and 500-1000 km s⁻¹ for slow, medium, and fast winds, respectively. The channels are chosen to ensure a sufficient number of data sets in each group, as shown in Table 1 (also see Appendix A for a distribution of the solar wind speeds).

To proceed with our analysis, we compute the density autocorrelation function for each data set using the Blackman–Tukey method (Blackman & Tukey 1958; as described in detail in Roy et al. 2021). The ensemble definition of the autocorrelation is

$$R(\tau) = \langle \rho(t)\rho(t+\tau)\rangle - \langle \rho(t)\rangle \langle \rho(t+\tau)\rangle, \tag{2}$$

where ρ is the ion density and τ is the time lag. Invoking the ergodic theorem, the brackets $\langle \cdots \rangle$ correspond formally to averaging over an infinite sample size. For finite data consisting of N equally spaced samples, we denote the averaging operation as $\langle \cdots \rangle'$. Specifically, for a data set $\{\rho_i\} = \rho_0, \cdots$, ρ_{N-1} with sampling time $\Delta t = 60$ s, τ takes integer multiples of Δt , and the averaging can be written explicitly as

$$\langle \rho(t) \rangle' = \langle \rho_i \rangle_{i=0,\dots,N-\tau/\Delta t-1},$$
 (3)

$$\langle \rho(t+\tau) \rangle' = \langle \rho_j \rangle_{j=\tau/\Delta t, \dots, N-1},$$
 (4)

$$\langle \rho(t)\rho(t+\tau)\rangle' = \langle \rho_j \rho_{j+\tau/\Delta t}\rangle_{j=0,\cdots,N-\tau/\Delta t-1}.$$
 (5)

For the remainder of the paper, for clarity, we drop the prime in the bracket notation.

For stationary data, $R(\tau)$ does not depend on the variable t, i.e., the origin of time. And therefore by definition, the correlation function is an even function of lag τ . Under appropriate conditions, this is equivalent to the Reynolds averaging expression for the correlation function, $R(\tau) = \langle \delta \rho(t) \delta \rho(t+\tau) \rangle$, where $\delta \rho(t) \equiv \rho(t) - \langle \rho(t) \rangle$ (see Germano 1992).

When we consider the normalized correlation function \hat{R} , the $R(\tau)$ resulting from Equation (2) is normalized by the data variance R(0):

$$\hat{R}(\tau) = \frac{R(\tau)}{R(0)}. (6)$$

To eliminate undersampled fluctuations at large lags, we pass each autocorrelation function through a 10% cosine taper window (Matthaeus & Goldstein 1982), where the last 10% of $\hat{R}(\tau)$ values are multiplied by the factor

$$\frac{1}{2} \left(1 + \cos \left[\frac{\pi}{0.1 \tau_{\text{max}}} (\tau - 0.9 \tau_{\text{max}}) \right] \right) \tag{7}$$

with $\tau_{\rm max}$ representing the maximum lag over which the autocorrelation is calculated. In this analysis the maximum lag is 4.8 hr; this corresponds to 1/5 of the data interval, and several times the anticipated correlation times.

We further transform the temporal lags τ into spatial lags λ by applying the Taylor frozen-in hypothesis (Taylor 1938), $\lambda = -V_{\rm SW}\tau$, where $V_{\rm SW}$ is the solar wind speed in the upstream direction averaged over the data interval. With this procedure, we arrive at a normalized, spatial lag-dependent correlation function $\hat{R}(\lambda)$.

4. Results

We first examine statistics of the density samples. The standard deviation over mean, otherwise known as the coefficient of variation, C.V., is a measure of the relative fluctuation amplitude of the density samples. The C.V. range up to 1.57 across the 24 hr data sets and increase with θ . Figure 1 illustrates the average sample C.V. with respect to θ and V_{SW} , with the error bars representing standard errors. These plots indicate that relative density fluctuations are stronger when the spacecraft samples flow perpendicular to, rather than parallel to, the mean magnetic field, and that slow wind exhibits slightly larger density fluctuations compared to fast wind. The top panel of Figure 1 is consistent with the recent work of Du et al. (2023), on the anisotropy of density fluctuations obtained from simulations of compressible MHD turbulence. We present further statistics of our density samples in Appendix B, which includes the standard deviation $\langle \delta \rho^2 \rangle^{1/2}$ of density for each angular and wind speed channel. It is well known that slow wind is denser than fast wind (McComas et al. 2000; Usmanov et al. 2018); it is shown in Appendix B that the density fluctuation magnitudes in slow wind are also larger. We also include a joint distribution of the density standard deviation and mean.

We proceed to our investigation of the correlation anisotropy. The normalized autocorrelation functions are averaged within each group of speed and angular channel, resulting in 21 instances of autocorrelations henceforth represented by $\hat{R}(\lambda = -V_{\rm SW}\tau)$. These are shown in the panels of Figure 2.

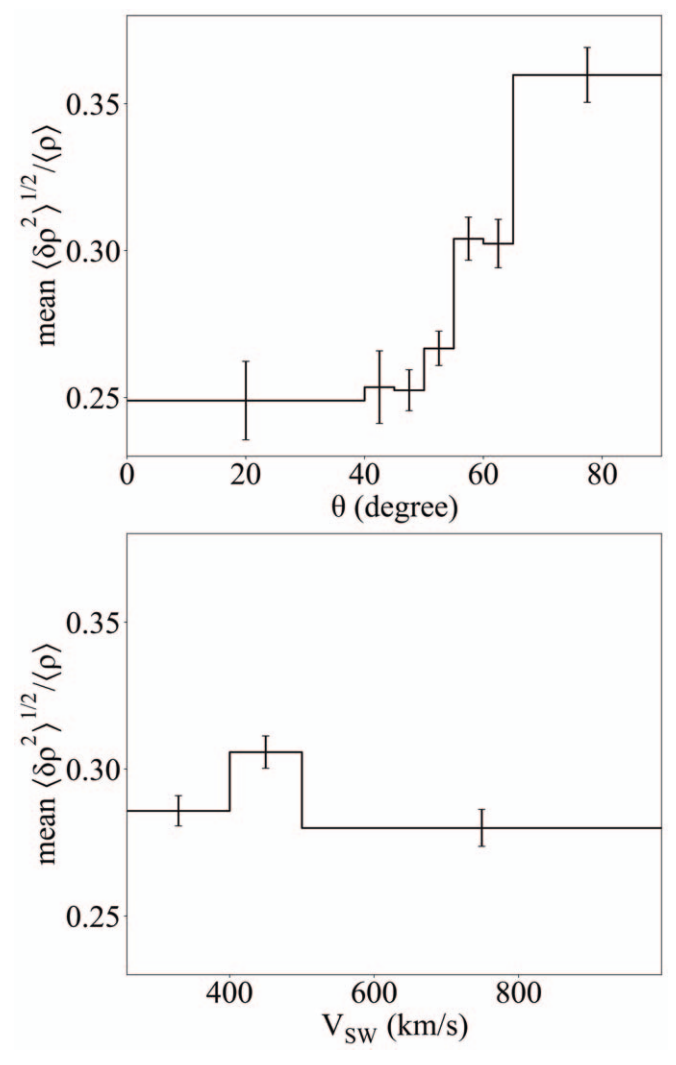


Figure 1. Density coefficient of variation averaged over each θ channel (top panel) and each $V_{\rm SW}$ channel (bottom panel). Error bars represent standard errors. Here $\delta \rho(t) \equiv \rho(t) - \langle \rho(t) \rangle$, where $\langle \cdots \rangle$ refers to an average over an individual 24 hr data set, and "mean" refers to averaging the coefficient of variations over all 24 hr data sets that lie within a θ or $V_{\rm SW}$ channel.

Separate panels correspond to slow, medium, and fast winds, and within each, angular variations are demonstrated.

The correlation length λ_c , defined as the spatial lag where the correlation decreases by a factor of 1/e, is listed in Table 2 for each channel. The uncertainties are standard errors calculated from the ensemble of intervals within each channel. We further plot λ_c over θ for all three wind channels in the top panel of Figure 3, and fit each set of data with a linear curve using least-squares analysis. We find a general subtle trend of correlation length decreasing as θ increases in both slow and medium wind —the slope of slow wind is negative with a 2σ confidence, as shown in the legend of Figure 3. However, the slope of fast wind is close to zero. This indicates that the longest average correlation lengths in slow and medium winds occur when the mean magnetic field direction is quasi-aligned with the plasma flow direction, while in fast wind the correlation lengths are approximately isotropic.

We also list, in parentheses in Table 2, the spatial lag where the correlation decreases by a factor of 1/2e, denoted as $\lambda_{1/2e}$. The corresponding plot is shown in the bottom panel of Figure 3. We find that as compared to λ_c , $\lambda_{1/2e}$ decreases more

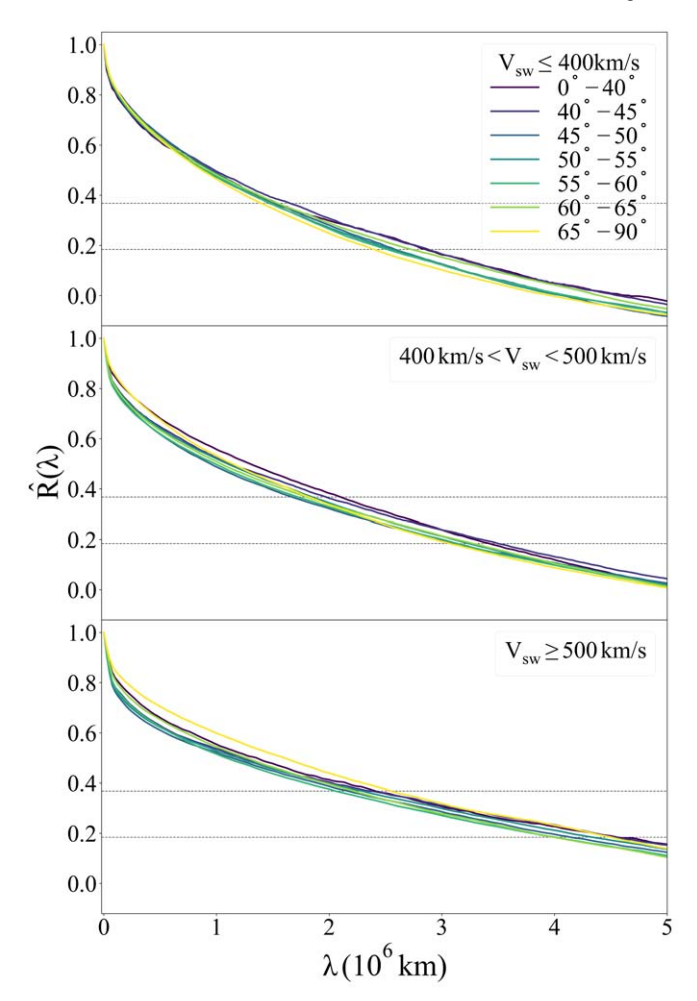


Figure 2. Normalized density autocorrelation for slow (top panel), medium (middle panel), and fast (bottom panel) winds as functions of spatial lag. The correlations have been averaged within each angular channel, denoted by distinctly colored lines. Dashed horizontal lines indicate where $\hat{R} = 1/e$ and 1/2e.

	\leq 400 km s ⁻¹	400–500 km s ⁻¹	\geqslant 500 km s ⁻¹
0°-40°	1.55 ± .17	$2.10 \pm .14$	$2.43 \pm .28$
	$(2.88 \pm .20)$	$(3.43 \pm .17)$	$(4.56 \pm .39)$
40°–45°	$1.65 \pm .15$	$1.98 \pm .13$	$2.38\pm.22$
	$(2.90 \pm .16)$	$(3.51 \pm .17)$	$(4.56 \pm .26)$
45°-50°	$1.53 \pm .09$	$1.68 \pm .07$	$2.18\pm.10$
	$(2.60 \pm .10)$	$(3.13 \pm .10)$	$(4.16 \pm .13)$
50°-55°	$1.48 \pm .07$	$1.85 \pm .06$	$2.30 \pm .07$
	$(2.58 \pm .08)$	$(3.26 \pm .07)$	$(4.36 \pm .09)$
55°-60°	$1.50 \pm .06$	$1.73 \pm .05$	$2.08 \pm .07$
	$(2.53 \pm .07)$	$(3.16 \pm .07)$	$(4.03 \pm .10)$
60°-65°	$1.55 \pm .07$	$1.80 \pm .06$	$2.23 \pm .11$
	$(2.75 \pm .08)$	$(3.28 \pm .08)$	$(4.01 \pm .14)$
65°-90°	$1.40 \pm .06$	$1.83 \pm .07$	$2.55\pm.18$
	$(2.40 \pm .07)$	$(3.08 \pm .09)$	$(4.51 \pm .24)$
Average	$1.52 \pm .27$	1.85 ± .24	2.31 ± .44
-	$(2.67 \pm .31)$	$(3.26 \pm .30)$	$(4.31 \pm .58)$

Note. The uncertainties represent standard errors. Spatial lags where correlation decreases by 1/2e are listed in parentheses.

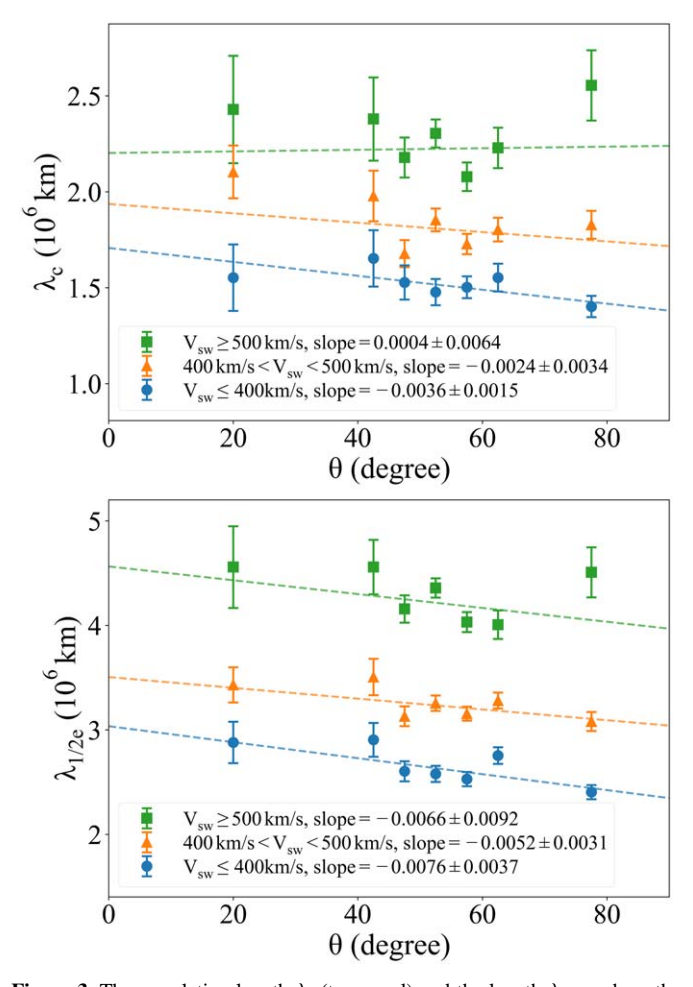


Figure 3. The correlation length λ_c (top panel) and the length $\lambda_{1/2e}$ where the correlation decreases by a factor of 1/2e (bottom panel) as functions of angular channel for slow, medium, and fast winds. The data and uncertainties are consistent with those listed in Table 2. Dashed lines show linear best fits with corresponding slopes listed in the legends.

noticeably as θ increases, suggesting that the observed correlation persists to larger distances in the parallel directions. Equivalently, the gradients at the outer scale of turbulence are moderately stronger in the perpendicular directions. Additionally, we observe that the correlation lengths are systematically longer in fast wind compared to slow wind. This latter difference appears to be clearer in density correlations compared with magnetic correlations (Weygand et al. 2011).

To better visualize the density correlation anisotropy for slow, medium, and fast winds, in Figure 4 we plot the contour levels of the averaged autocorrelations $\hat{R}(\lambda)$ in perpendicular and parallel lag spaces through the transformation $(\lambda_{\perp} = \lambda \sin \theta, \, \lambda_{\parallel} = \lambda \cos \theta)$, following Dasso et al. (2005). The contours are computed in the first quadrant, then mirrored about the $\theta=0^{\circ}$ and 90° axes under symmetry assumptions. This is a statistical demonstration of the "Maltese cross" geometry in density fluctuation fields.

It is evident that the outermost contours of constant correlation in Figure 4, those with the smallest correlation values, are slightly elongated in the parallel direction for slow and medium wind speed. These contours of very low correlation values (the largest "circles") may be characterized as weakly "2D-like" in the sense described in Dasso et al. (2005), whereas the fast wind contour is isotropic. However,

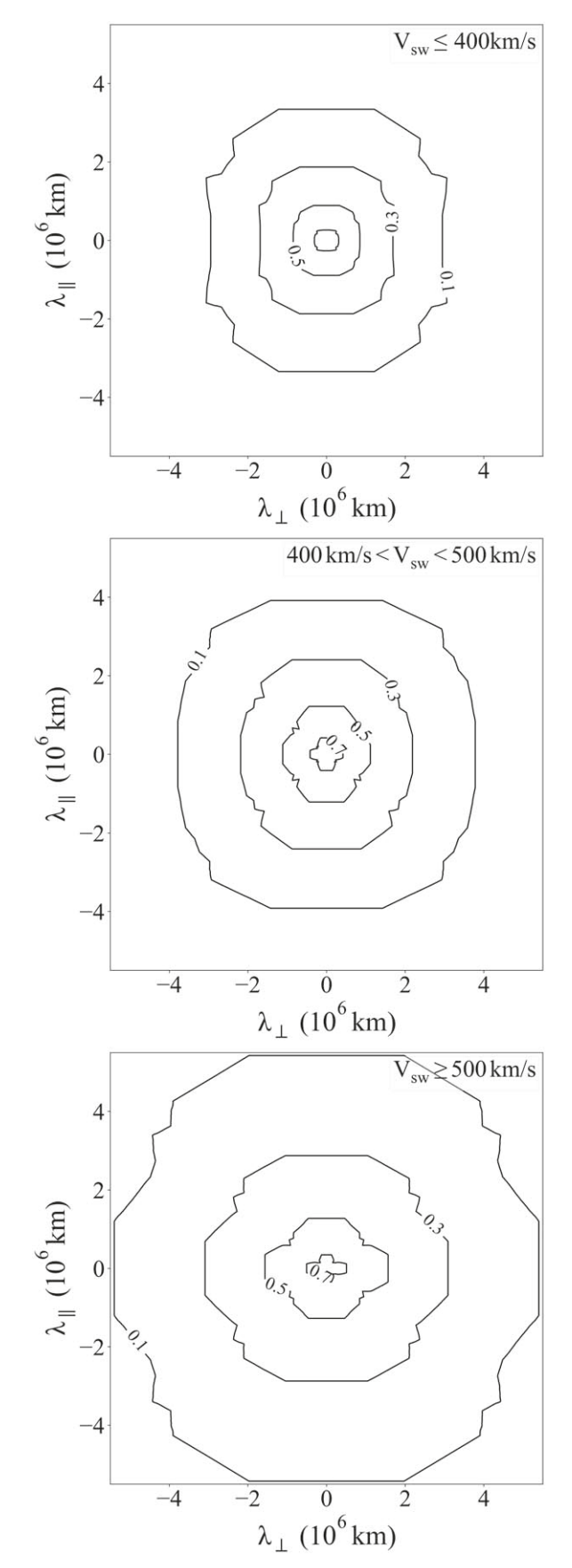


Figure 4. The correlation contours for slow (top panel), medium (medium panel), and fast (bottom panel) winds, calculated from Figure 2 through the transformation ($\lambda_{\perp} = \lambda \sin \theta$, $\lambda_{\parallel} = \lambda \cos \theta$).

Table 3 Estimates of λ_{\perp} and λ_{\parallel} in Units of 10^6 km as Well as Their Ratio on the Correlation Contours $\hat{R}(\lambda)=0.9,\,0.7,\,0.5,\,1/e,\,0.3,\,1/2e,$ and 0.1 for Slow, Medium, and Fast Winds

	Ŕ	λ_{\perp}	λ_{\parallel}	$\lambda_{\perp}/\lambda_{\parallel}$
	0.9	0.04	0.02	1.67
	0.7	0.31	0.26	1.17
	0.5	0.85	0.89	0.95
\leq 400 km s ⁻¹	1/e	1.37	1.45	0.94
	0.3	1.69	1.87	0.90
	1/2e	2.34	2.69	0.87
	0.1	2.95	3.34	0.88
	0.9	0.05	0.04	1.15
	0.7	0.42	0.42	1.00
	0.5	1.11	1.22	0.91
$400-500 \text{ km s}^{-1}$	1/e	1.78	1.97	0.90
	0.3	2.18	2.41	0.91
	1/2e	3.00	3.22	0.93
	0.1	3.78	3.92	0.97
	0.9	0.05	0.04	1.30
	0.7	0.51	0.35	1.47
	0.5	1.57	1.27	1.23
\geqslant 500 km s ⁻¹	1/e	2.49	2.27	1.10
	0.3	3.09	2.87	1.08
	1/2e	4.39	4.28	1.03
	0.1	5.40	5.42	1.00

the higher correlation contours (the smaller circles) tend to exhibit the opposite type of anisotropy that may be described as "slablike." Specifically, for fast wind, the contours with correlation greater than 0.1 is somewhat "slablike" with elongation in the perpendicular direction, and this tendency becomes more pronounced at higher correlation values, as depicted in the bottom panel of Figure 4. Meanwhile, the $\hat{R}=0.5$ contours for slow and intermediate winds remain slightly 2D-like, even though they also become slablike at the highest correlation values. This general tendency of the correlation contours in its dependence on wind speed is qualitatively consistent with the magnetic field results from Dasso et al. (2005). We discuss this comparison in greater detail later.

The general increase in correlation lengths with increasing wind speed is also readily apparent in Figure 4, where isocontours "expand" from the top to the bottom panel.

Table 3 quantifies the density anisotropies as we have described above. Here, we list the values for λ_{\perp} , λ_{\parallel} , and $\lambda_{\perp}/\lambda_{\parallel}$ in all three wind speed channels corresponding the following normalized correlations: $\hat{R} = 0.9, 0.7, 0.5, 1/e, 0.3, 1/2e$, and 0.1. Scales larger than the correlation scale are considered the energy-containing scale, while smaller scales belong to the inertial range. The lags are calculated from Figure 2 using $\lambda_{\perp} = \lambda(\hat{R}_{65^{\circ}-90^{\circ}})\sin 77.5^{\circ}$ and $\lambda_{\parallel} = \lambda(\hat{R}_{0^{\circ}-40^{\circ}})\cos 20^{\circ}$, or can be directly observed in Figure 4. Note that due to the coarse binning at low θ , λ_{\parallel} may be underestimated and $\lambda_{\perp}/\lambda_{\parallel}$ may be overestimated. Figure 5 shows how $\lambda_{\perp}/\lambda_{\parallel}$ varies with \hat{R} . We again observe that the correlations are slightly elongated along the parallel direction at small \hat{R} (large spatial lags), while for small spatial lags (large \hat{R}), corresponding to the inertial range, the correlations are elongated in the perpendicular direction. The systematic underestimation of parallel correlation lengths

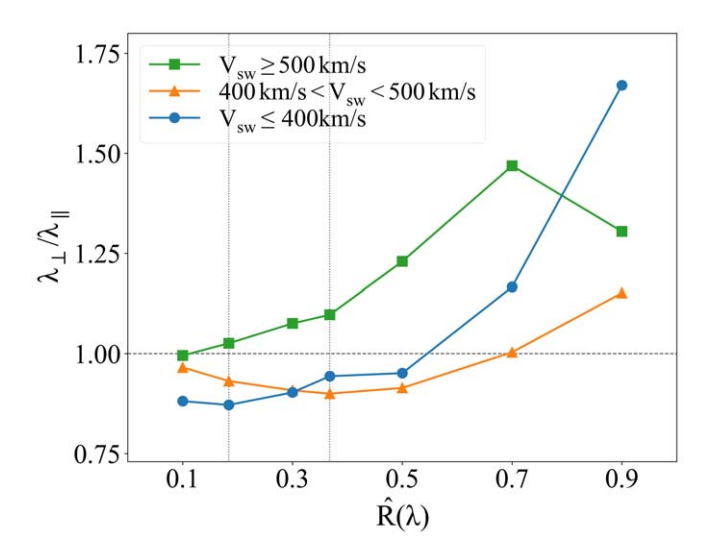


Figure 5. Estimates of $\lambda_{\perp}/\lambda_{\parallel}$ as functions of $\hat{R}(\lambda)$ for slow, medium, and fast winds. Dotted vertical lines indicate the 1/e and 1/2e correlation levels. Dashed horizontal line indicates where $\lambda_{\perp}/\lambda_{\parallel}=1$.

suggests that the dynamics may be more 2D-like than predicted in Figures 4 and 5.

5. Discussion

There is a general tendency for MHD, and plasma turbulence in the MHD range of scales as well, to exhibit correlation anisotropy, and equivalently, spectral anisotropy relative to the direction of a regional mean magnetic field of sufficient strength (Shebalin et al. 1983; Oughton et al. 1994). Other effects may also introduce anisotropies by imposing preferred directions that influence regional and local dynamics. For example, in a structured and expanding medium such as the solar wind, large-scale plasma flows may introduce preferred directions that influence anisotropy. A notable effect is that of expansion, which, in the simplest case, selects the radial direction as preferred. Other relevant effects include regions of shear and compression occurring between high- and low-speed streams and near shocks, as well as interactions involving structures such as coronal mass ejections. One may expect that these various influences on anisotropy may operate at different length scales, and may have varying levels of influence on different physical quantities. For mostly practical reasons, solar wind studies on turbulence anisotropy have often concentrated on the magnetic field. The present report extends this discussion to include the fluctuations in density.

More specifically, most previous examinations of anisotropy have considered the relatively local effects of the magnetic field direction on the rotational symmetry of magnetic fluctuations (Bieber et al. 1994, 1996). Based on results from laboratory experiments (Robinson & Rusbridge 1971) and numerical simulations (Shebalin et al. 1983; Oughton et al. 1994), the expectation is that MHD-scale turbulence will display a Q2D anisotropy relative to the field direction. This expectation is mainly motivated by a property of incompressive dynamics, namely that the cascade to higher perpendicular wavenumbers proceeds unabated while the parallel cascade is inhibited by wave propagation (Shebalin et al. 1983). This anisotropy is reasonably well confirmed in most analyses of solar wind rotational symmetry (Bieber et al. 1994, 1996). An exception is the study of Saur & Bieber (1999), which finds some support

for a preferred role of the radial direction at relatively lower frequencies. The later finding suggests the influence of expansion, an effect clearly seen in WKB treatments (e.g., Völk & Aplers 1973).

Considering a broader context, the dynamics in the solar wind at 1 au may consist of an admixture of incompressive and compressive parts. In this more realistic portrayal, more complex influences on rotational symmetry may be anticipated. In particular, the incompressive tendency toward a Q2D configuration merges with the relatively isotropic spectral (and correlation) statistics attributed to the compressible dynamics. Indeed, compressible MHD simulations (Matthaeus et al. 1996; Du et al. 2023) with Mach number, plasma β , and $\delta B/B$ similar to those of the solar wind indicate that density spectra are anisotropic, but less so than the anisotropy seen in incompressible simulations (Oughton et al. 1994). This appears to be consistent with the current findings in slow and medium winds, wherein the correlation lengths parallel and perpendicular to the mean magnetic field differ from one another by only a small relative fraction. The present finding also suggests a more complex scenario in which the sense of anisotropy varies across scales.

It has been previously suggested (Dasso et al. 2005; Weygand et al. 2011) that for the magnetic field in the solar wind, the parallel correlation scale is larger than the perpendicular correlation scale by a factor of around 2 for the slow solar wind. This is a modest 2D-like anisotropy compared to what is expected at smaller scales in the inertial range. However, such a ratio is considerably larger than that of the density correlation scales reported here.

Here, for density fluctuations, the sense of anisotropy at the correlation scale, whether measured at the 1/e or the 1/2e level, is mainly of the "2D" type. (The fast wind is essentially isotropic at the 1/e scale but becomes slightly 2D at larger scales.) We suggest that the weaker outer-scale anisotropy of the density is due to the effects of the admixture of more anisotropic incompressive turbulence with less anisotropic compressible turbulence, consistent with previous numerical results (see, e.g., Figure 5 of Matthaeus et al. 1996).

It is interesting, perhaps a bit surprising and of potential significance, that at smaller scales (higher correlation values), the sense of density anisotropy reverses and favors slablike symmetries. This trend occurs in all wind speed channels and is especially dramatic for fast wind. This is reminiscent of the sense of magnetic anisotropy at correlation scales in fast wind (Dasso et al. 2005). Furthermore, by inspection of the magnetic correlation contours in Dasso et al. (2005), it appears that slablike symmetry occurs across a wide range of scales in fast wind. This, however, was not quantified. But for slow wind, the 2D-like sense of magnetic anisotropy mentioned above as present at the correlation scale remains (as seen by inspection) 2D-like over a reasonably wide range of scales. Furthermore, in the above-quoted compressible MHD simulation results (Matthaeus et al. 1996), the inertial range contours of density spectra appear to be of the 2D type, although not dramatically so. Finally, we note that our finding of slablike density in the fast wind inertial range also seems to contradict Figure 5 and 6 of Chen et al. (2012), who use Ulysses data and adopt |B| as a proxy for compressive fluctuations. A major difference, however, is that the analysis of Chen et al. (2012) is carried out in a coordinate system based on a local definition of the mean field. Such a procedure systematically increases the ratio

of perpendicular to parallel structure functions, thus favoring 2D-like interpretations (Matthaeus et al. 2012). Our computation of mean fields integrated over longer times is chosen to avoid this bias.

We cannot rule out the appearance of field-aligned (2D-like) anisotropies at much smaller scales, possibly for all wind speeds. Indeed, these are favored by coronal observations such as Armstrong et al. (1990). The study found field-aligned elongated structures having anisotropy ratios that increase with increasing heliocentric distance from 2 to about 10 solar radii. However, these observations were at much smaller scales, and much closer to the Sun, relative to the present large-scale observations at 1 au. Nevertheless, these authors did suggest that solar wind density anisotropy varies with scale. On the other hand, Zank et al. (2024) studied density fluctuations in sub-Alfvénic wind using mode-decomposition analysis, and found anisotropy dominated by a combination of the slablike entropy mode and the 2D-like backward propagating slow magnetosonic mode. The anisotropy of their entropy mode is consistent with our results, although their results extend over the scales $k = 2 \times 10^{-6}$ to 10^{-2} km⁻¹, which slightly overlaps with the smallest scales we investigate.

The present results for the anisotropy of density stand in substantial contrast to expectations based on magnetic and velocity field spectra in incompressible simulations and in solar wind observations. The basis of this expectation is that the incompressible cascade, which presumably is a major factor in the solar wind dynamics, is well known to favor 2D-like anisotropies (Oughton et al. 2015). The reasons for this departure remain unclear at present, but most likely pertain to the way compressible fluctuations are generated in the solar wind. Further research will be required to arrive at a clearer understanding.

Future observations from the PUNCH mission (Deforest et al. 2022) will provide us with solar wind density data in regions of the inner heliosphere yet unexplored and with an unprecedented field of view. As observed in DeForest et al. (2016), the solar wind shows a transition from "striated" to "flocculated" features, suggesting an evolution toward isotropization (Cuesta et al. 2022). Using the white-light images obtained from PUNCH, it will be possible to recover unprecedented mapping of solar wind density. Such measurements will be used to perform analyses similar to those presented in this paper, which will provide invaluable knowledge about the radial evolution of solar wind anisotropy.

Acknowledgments

The velocity and density data were downloaded from https://spdf.gsfc.nasa.gov/pub/data/ace/swepam/level2_hdf/ions_64sec. This research is partially supported by the NASA LWS grant 80NSSC20K0377 (subcontract 655-001), and by the NASA IMAP project at UD under subcontract SUB0000317 from Princeton University. R.C. and M.E.C. acknowledge LANL's hospitality during Summer 2022, when part of this work was performed.

Appendix A Distribution of Solar Wind Speed at 1 au

The separation of data intervals into three wind speed classes is a central part of this analysis. To ensure a reasonable level of statistical validity in each class, we base the partitioning by

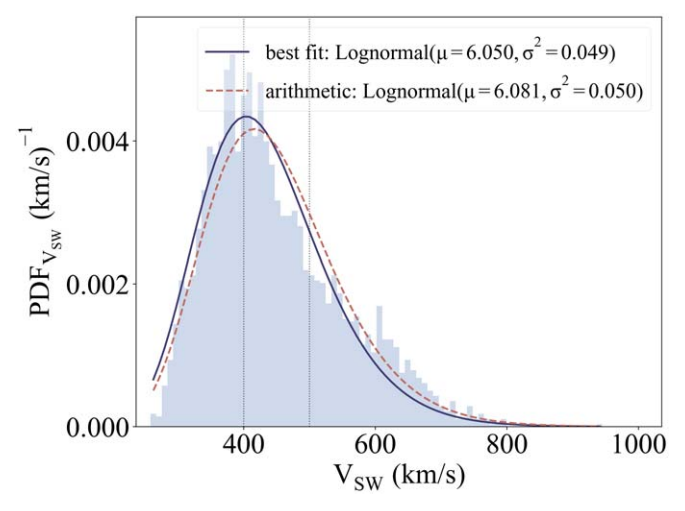


Figure 6. Shaded histogram shows the distribution of solar wind speeds. Dotted vertical lines represent the boundaries of the solar wind speed channels. Solid curve shows the best-fit lognormal distribution. Dashed curve shows the lognormal distribution derived from the arithmetic mean and variance of the wind speed samples. Parameters of both lognormal distributions are listed in the legend.

speed on an understanding of its probability distribution, as shown in Figure 6. The boundaries for slow, medium, and fast wind channels are represented by dotted vertical lines to show an almost equal number of counts in each channel.

Appendix B Statistics of Solar Wind Density at 1 au

Here, we provide further statistics on our density samples. The standard deviation, S.D., measures the fluctuation amplitude, as opposed to the relative fluctuation amplitude shown in Figure 1. Figure 7 shows the average S.D. of the

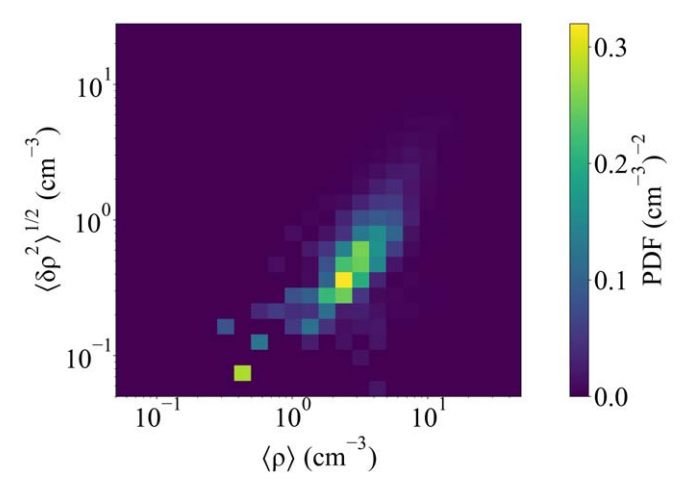


Figure 8. 2D distribution of density standard deviation and mean. Data from all θ and $V_{\rm SW}$ channels are combined.

density samples with respect to θ and $V_{\rm SW}$, with error bars representing standard errors. The S.D. values range from 0.6 to 3.4 cm⁻³ across the 24 hr data sets, and increase with θ and decrease with $V_{\rm SW}$. By comparing Figures 1 and 7, we note that the trend of the density fluctuation amplitude increasing with the angle between the magnetic and velocity fields is not compensated by the increasing mean density. Whereas the tendency toward higher fluctuation amplitude in slower winds is predominantly ascribed to a corresponding increase in mean density.

To study the relationship between mean density and density fluctuation in the solar wind at 1 au, we plot in Figure 8 the joint probability density of the two variables. As expected, we observe larger mean densities corresponding to greater fluctuations.

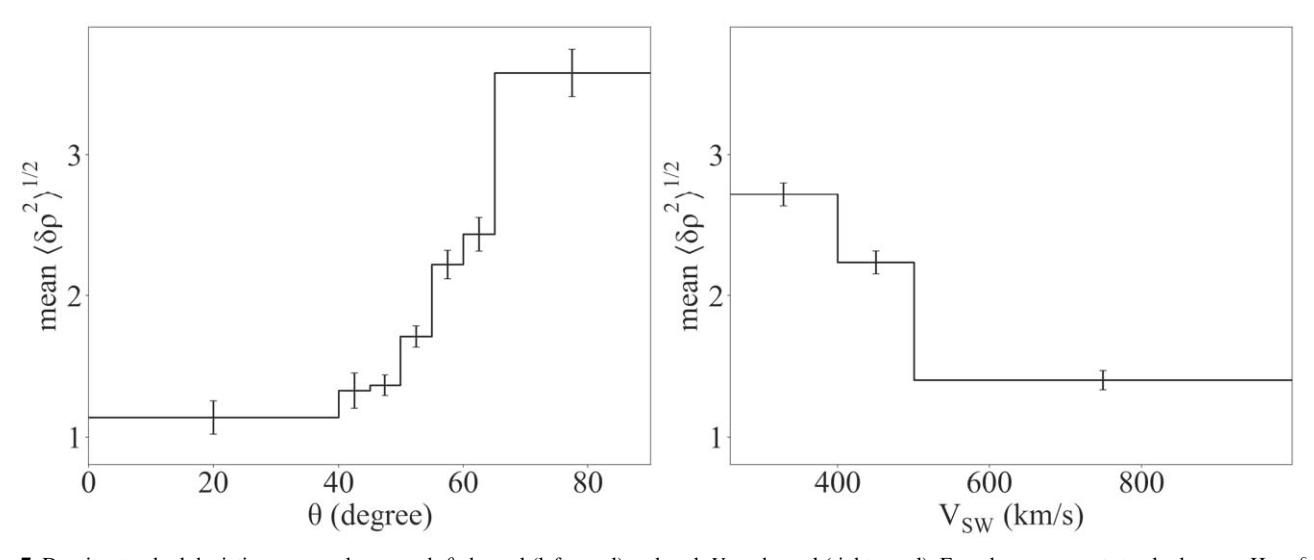


Figure 7. Density standard deviation averaged over each θ channel (left panel) and each $V_{\rm SW}$ channel (right panel). Error bars represent standard errors. Here $\delta\rho(t) \equiv \rho(t) - \langle \rho(t) \rangle$, where $\langle \cdots \rangle$ refers to an average over an individual 24 hr data set, and "mean" refers to averaging the coefficient of variations over all 24 hr data sets that lie within a θ or $V_{\rm SW}$ channel.

ORCID iDs

Jiaming Wang https://orcid.org/0009-0008-8723-610X Rohit Chhiber https://orcid.org/0000-0002-7174-6948 Sohom Roy https://orcid.org/0000-0003-3891-5495 Manuel E. Cuesta https://orcid.org/0000-0002-7341-2992 Francesco Pecora https://orcid.org/0000-0003-4168-590X Yan Yang https://orcid.org/0000-0003-2965-7906 Xiangrong Fu https://orcid.org/0000-0002-4305-6624 Hui Li https://orcid.org/0000-0003-3556-6568 William H. Matthaeus https://orcid.org/0000-0001-7224-6024

```
References
Adhikari, L., Zank, G. P., Hunana, P., et al. 2017, ApJ, 841, 85
Armstrong, J. W., Coles, W. A., Kojima, M., & Rickett, B. J. 1990, ApJ,
  358, 685
Balmaceda, L. A., Solanki, S. K., Krivova, N. A., & Foster, S. 2009, JGRA,
   114, A07104
Barnes, A. 1981, JGR, 86, 7498
Barnes, A., & Hollweg, J. V. 1974, JGR, 79, 2302
Batchelor, G. K. 1970, The Theory of Homogeneous Turbulence (Cambridge:
   Cambridge Univ. Press)
Bellamy, B. R., Cairns, I. H., & Smith, C. W. 2005, JGR, 110, A10104
Bieber, J. W., Matthaeus, W. H., Smith, C. W., et al. 1994, ApJ, 420, 294
Bieber, J. W., Wanner, W., & Matthaeus, W. H. 1996, JGR, 101, 2511
Blackman, R. B., & Tukey, J. W. 1958, The Measurement of Power Spectra
   (New York: Dover)
Borovsky, J. E. 2012, JGRA, 117, A05104
Bruno, R., & Carbone, V. 2013, LRSP, 10, 2
Cane, H. V., & Richardson, I. G. 2003, JGRA, 108, 1156
Celnikier, L. M., Muschietti, L., & Goldman, M. V. 1987, A&A, 181, 138
Chandran, B. D. G. 2005, PhRvL, 95, 265004
Chandran, B. D. G., & Backer, D. C. 2002, ApJ, 576, 176
Chen, C. H. K., Mallet, A., Schekochihin, A. A., et al. 2012, ApJ, 758, 120
Chen, C. H. K., Mallet, A., Yousef, T. A., Schekochihin, A. A., &
   Horbury, T. S. 2011, MNRAS, 415, 3219
Chen, C. H. K., Boldyrev, S., Xia, Q., & Perez, J. C. 2013, PhRvL, 110,
Cho, J., & Lazarian, A. 2002, PhRvL, 88, 245001
Cho, J., Lazarian, A., & Vishniac, E. T. 2002, ApJ, 564, 291
Coles, W. A., & Harmon, J. K. 1989, ApJ, 337, 1023
Cuesta, M. E., Chhiber, R., Roy, S., et al. 2022, ApJL, 932, L11
Dasso, S., Milano, L. J., Matthaeus, W. H., & Smith, C. W. 2005, ApJL, 635, L181
Deforest, C., Killough, R., Gibson, S., et al. 2022, in 2022 IEEE Aerospace
   Conference (AERO) (Piscataway, NJ: IEEE), 1
DeForest, C. E., Matthaeus, W. H., Viall, N. M., & Cranmer, S. R. 2016, ApJ,
Du, S., Li, H., Gan, Z., & Fu, X. 2023, ApJ, 946, 74
Frisch, U. 1995, Turbulence: the legacy of AN Kolmogorov (Cambridge:
   Cambridge Univ. Press)
```

```
Gan, Z., Li, H., Fu, X., & Du, S. 2022, ApJ, 926, 222
Germano, M. 1992, JFM, 238, 325
Goldreich, P., & Sridhar, S. 1995, ApJ, 438, 763
Hamilton, K., Smith, C. W., Vasquez, B. J., & Leamon, R. J. 2008, JGRA, 113,
Horbury, T. S., Wicks, R. T., & Chen, C. H. K. 2012, SSRv, 172, 325
Kellogg, P. J., & Horbury, T. S. 2005, AnGeo, 23, 3765
Klein, L. W., & Burlaga, L. F. 1982, JGR, 87, 613
Kontar, E. P., Emslie, A. G., Clarkson, D. L., et al. 2023, ApJ, 956, 112
Malaspina, D. M., Kellogg, P. J., Bale, S. D., & Ergun, R. E. 2010, ApJ,
  711, 322
Matthaeus, W. H., Ghosh, S., Oughton, S., & Roberts, D. A. 1996, JGR,
   101, 7619
Matthaeus, W. H., & Goldstein, M. L. 1982, JGR, 87, 6011
Matthaeus, W. H., Goldstein, M. L., & Roberts, D. A. 1990, JGR, 95, 20673
Matthaeus, W. H., Servidio, S., Dmitruk, P., et al. 2012, ApJ, 750, 103
McComas, D. J., Bame, S. J., Barker, P., et al. 1998, SSRv, 86, 563
McComas, D. J., Barraclough, B. L., Funsten, H. O., et al. 2000, JGR, 105,
Narita, Y., Glassmeier, K. H., Sahraoui, F., & Goldstein, M. L. 2010, PhRvL,
   104, 171101
Oughton, S., & Matthaeus, W. H. 2020, ApJ, 897, 37
Oughton, S., Matthaeus, W. H., Wan, M., & Osman, K. T. 2015, RSPTA, 373,
Oughton, S., Priest, E. R., & Matthaeus, W. H. 1994, JFM, 280, 95
Panchev, S. 1971, Random Functions and Turbulence (New York: Pergamon)
Richardson, I., & Cane, H. 2024, Near-Earth Interplanetary Coronal Mass
  Ejections Since January 1996, V2, Harvard Dataverse, doi:10.7910/DVN/
Robinson, D. C., & Rusbridge, M. G. 1971, PhFl, 14, 2499
Roy, S., Chhiber, R., Dasso, S., Ruiz, M. E., & Matthaeus, W. H. 2021, ApJL,
  919, L27
Saur, J., & Bieber, J. W. 1999, JGR, 104, 9975
Shaikh, D., & Zank, G. P. 2010, MNRAS, 402, 362
Shalchi, A. 2009, Nonlinear Cosmic Ray Diffusion Theories (Berlin: Springer)
Shalchi, A., Li, G., & Zank, G. P. 2010, Ap&SS, 325, 99
Shebalin, J. V., Matthaeus, W. H., & Montgomery, D. 1983, JPIPh, 29, 525
Smith, C. W., L'Heureux, J., Ness, N. F., et al. 1998, SSRv, 86, 613
Taylor, G. I. 1938, RSPSA, 164, 476
Usmanov, A. V., Matthaeus, W. H., Goldstein, M. L., & Chhiber, R. 2018,
    ApJ, 865, 25
Völk, H. J., & Aplers, W. 1973, Ap&SS, 20, 267
Weygand, J. M., Matthaeus, W. H., Dasso, S., & Kivelson, M. G. 2011, JGRA,
  116, A08102
Zank, G. P., Jetha, N., Hu, Q., & Hunana, P. 2012, ApJ, 756, 21
Zank, G. P., Li, G., Florinski, V., et al. 2004, JGRA, 109, A04107
Zank, G. P., Zhao, L. L., Adhikari, L., et al. 2023, ApJS, 268, 18
Zank, G. P., Zhao, L. L., Adhikari, L., et al. 2024, ApJ, 966, 75
Zhao, L. L., Adhikari, L., Zank, G. P., Hu, Q., & Feng, X. S. 2017, ApJ,
  849, 88
Zhao, L. L., Adhikari, L., Zank, G. P., Hu, Q., & Feng, X. S. 2018, ApJ,
```

Zhao, L. L., Zank, G. P., Nakanotani, M., & Adhikari, L. 2023, ApJ, 944, 98